Inorg. Chem. **1996,** *35,* 4323−4335

Excited-State Distortions and Electron Delocalization in Mixed-Valence Dimers: Vibronic Analysis of the Near-IR Absorption and Resonance Raman Profiles of $[Fe_2(OH)_3(tmtacn)_2]^{2+}$

Daniel R. Gamelin,[†] **Emile L. Bominaar,**[‡] **Corine Mathonière,**[§] **Martin L. Kirk,**[†]
Karl Wieghardt,[||] **Jean-Jacques Girerd,**[§] **and Edward I. Solomon***[,†]

Department of Chemistry, Stanford University, Stanford, California 94305, Department of Chemistry, Carnegie Mellon University, Pittsburgh, Pennsylvania 15213, Laboratoire de Chimie Inorganique, URA CNRS 420, Institut de Chimie Moléculaire d'Orsay, Université de Paris-Sud, 91405 Orsay, France, and Max-Planck-Institut für Strahlenchemie, Stiftstrasse 34-36, D-45470 Mülheim an der Ruhr, Germany

Received April 17, 1996[⊗]

The near-IR transition associated with valence delocalization in the class III mixed-valence dimer $[Fe_2(OH)_3(tmtacn)_2]^{2+}$ is studied using variable-temperature (VT) electronic absorption and resonance Raman (RR) spectroscopies to gain insight into the properties of electron delocalization in this dimer. Laser excitation into this absorption band leads to dominant resonance Raman enhancement of totally-symmetric $[Fe_2(OH)_3]^{2+}$ core vibrational modes at 316 and 124 cm^{-1}, descriptions of which are calculated from a normal coordinate analysis. Vibronic analysis of the near-IR resonance Raman excitation profiles and VT-absorption bandshapes using an anharmonic excited-state model provides a description of the geometric distortions accompanying this excitation. The excited-state distortion is dominated by expansion of the $[Fe_2(OH)_3]^{2+}$ core along the Fe···Fe axis, reflecting the significant Fe−Fe $\sigma \rightarrow \sigma^*$ character of this transition. The ground-state σ-interaction between the two metals has been identified as the orbital pathway for valence delocalization, and the $\sigma \rightarrow \sigma^*$ distortion analysis is used to quantify the structural dependence of the electronic-coupling matrix element, H_{AB}, associated with this pathway. The dominant role of totally-symmetric nuclear coordinates in the absorption and RR spectroscopies of $[Fe_2(OH)_3(tmtacn)_2]^{2+}$ is also discussed in relation to the Q_- vibrational coordinate and the vibronic spectroscopies of other class II and class III mixed-valence dimers. It is shown that intensity contributions from the Q_- coordinate to the absorption and RR spectra of $[Fe_2(OH)_3(tmtacn)_2]^{2+}$ are small relative to those of the totally-symmetric coordinates due to the inefficient change-in-curvature mechanism by which the Q_- coordinate gains intensity, compared to the efficient excited-state displacement mechanism allowed for totally-symmetric coordinates. This is in contrast with the dominance of the Q_- coordinate over other totally-symmetric coordinates observed in intervalence transfer (IT) absorption and RR spectroscopies of class II mixed-valence complexes.

Introduction

Much attention has been focused on understanding the information content of absorption spectra of mixed-valence dimers.[1−8] In electronically-coupled valence-*localized* (class II) dimers, metal-to-metal charge transfer (MMCT, or intervalence transfer (IT)) dimer absorption features may be observed that correspond to optically-induced electron transfer between the two metals. As electronic coupling is increased, the description of this absorption process evolves to one of electron promotion between bonding and antibonding (or nonbonding depending on bridging ligation[7]) dimer wavefunctions (class III mixed-valence bonding-to-antibonding, $\psi \rightarrow \psi^*$). In the symmetric class III limit, this transition involves little or no net displacement of charge, and consequently such excitations show little change in static electric-dipole moment, as monitored by solvatochromism or electroabsorption experiments.[9,10]

The mixed-valence dimer $[Fe_2(OH)_3(tmtacn)_2]^{2+}$ has been shown by magnetic Mössbauer and L-edge X-ray absorption techniques to be in the class III limit of strong valence delocalization.[11−13] A detailed molecular orbital analysis of this dimer based on low-temperature (LT) electronic absorption, magnetic circular dichroism (MCD), and resonance Raman (RR) spectroscopies has shown the pathway for valence delocalization to involve a significant d_{z^2}–d_{z^2} σ-bonding interaction between the two irons, which gives rise to an intense Fe−Fe $\sigma \rightarrow \sigma^*$ ($a_1'(t_{2g}) \rightarrow a_2''(t_{2g})$ one-electron excitation) feature at ~13 500 cm^{-1} in the absorption and MCD spectra of this dimer.[14] The

---

[†] Stanford University.

[‡] Carnegie Mellon University.

[§] Université de Paris-Sud.

[||] Max-Planck-Institut für Strahlenchemie.

[⊗] Abstract published in *Advance ACS Abstracts,* June 15, 1996.

(1) *Mixed Valency Systems: Applications in Chemistry, Physics, and Biology*; Prassides, K., Ed.; Kluwer Academic Publishers: Dordrecht, The Netherlands, 1991.

(2) *Mechanistic Aspects of Inorganic Reactions*; Rorabacher, D. B., Endicott, J. F., Eds.; ACS Symposium Series 198; American Chemical Society: Washington, DC, 1982.

(3) *Mixed-Valence Compounds*; Brown, D. B., Ed.; Reidel: Dordrecht, The Netherlands, 1980.

(4) Piepho, S. B.; Krausz, E. R.; Schatz, P. N. *J. Am. Chem. Soc.* **1978**, *100*, 2996−3005.

(5) Wong, J. Y.; Schatz, P. N. *Prog. Inorg. Chem.* **1981**, *28*, 369−449.

(6) Ko, J.; Ondrechen, M. J. *Chem. Phys. Lett.* **1984**, *112*, 507−512.

(7) Ondrechen, M. J.; Ko, J.; Zhang, L.-T. *J. Am. Chem. Soc.* **1987**, *109*, 1672−1676.

(8) Piepho, S. B. *J. Am. Chem. Soc.* **1990**, *112*, 4197−4206.

(9) Oh, D. H.; Sano, M.; Boxer, S. G. *J. Am. Chem. Soc.* **1991**, *113*, 6880−6890.

(10) Reimers, J. R.; Hush, N. S. In ref 1, pp 29−50.

(11) Drüeke, S.; Chaudhuri, P.; Pohl, K.; Wieghardt, K.; Ding, X.-Q.; Bill, E.; Sawaryn, A.; Trautwein, A. X.; Winkler, H.; Gurman, S. J. *J. Chem. Soc., Chem. Commun.* **1989**, 59−62.

(12) Ding, X.-Q.; Bominaar, E. L.; Bill, E.; Winkler, H.; Trautwein, A. X.; Drüeke, S.; Chaudhuri, P.; Wieghardt, K. *J. Chem. Phys.* **1990**, *92*, 178−186.

(13) Peng, G.; van Elp, J.; Jang, H.; Que, L., Jr.; Armstrong, W. H.; Cramer, S. P. *J. Am. Chem. Soc.* **1995**, *117*, 2515−2519.

S0020-1669(96)00413-2 CCC: $12.00

energy of this transition is directly related to the inter-ion electronic-coupling matrix element, H_{AB}, of Marcus-Hush theory ($E_{\sigma\to\sigma^*} = 2H_{AB}$).[15,16]

In this study a combination of VT electronic absorption, resonance Raman, and quantitative bandshape analysis including anharmonic effects is used to describe the distorted $\sigma \to \sigma^*$ excited state relative to the ground-state equilibrium geometry. The resulting description confirms the assignment of this feature and, more importantly, provides a quantitative measure of the energetics of valence delocalization in this dimer. From the detailed vibronic analysis of this near-IR absorption band an experimental description is developed of the roles of symmetric (Q_{sym}) and antisymmetric (Q_-) vibrational normal coordinates in this class III mixed-valence dimer, and this is related to the absorption and resonance Raman spectroscopies of other mixed-valence dimers.

Experimental Section

$[C_{18}H_{45}N_6O_3Fe_2][ClO_4]_2 \cdot 2CH_3OH \cdot 2H_2O$ was prepared as described in ref 11, and isotopically labeled using ~63% ^{18}O enrichment in this procedure.

Variable-Temperature Electronic Absorption Spectroscopy. Low-temperature and variable-temperature absorption data were collected on a Cary-17 spectrophotometer. Temperature control was obtained using a Janis Research Super Vari-Temp cryogenic dewar mounted in the optical path. Temperatures between 2 and 300 K are measured to within ~1 K accuracy using a calibrated silicon diode (DT-500P) sensor mounted in close proximity to the sample on the sample rod. $[Fe_2(OH)_3(tmtacn)_2]^{2+}$, dissolved anaerobically in 50:50 propionitrile:butyronitrile solvent mixtures deoxygenated by multiple freeze−pump−thaw cycles, was injected into absorption sample cells comprised of quartz disks separated by Viton o-ring spacers, and rapidly frozen. Solid-state spectra were collected using powdered sample suspended in poly(dimethylsiloxane) mulling agent between quartz disks.

Vibrational and Resonance Raman Spectroscopy. Resonance Raman spectra were obtained using CW excitation from Kr^+ (Coherent I90K) and Ar^+ (Coherent I18UV) ion laser sources. Incident power in the range of 15−75 mW was used in a ~135° backscattering arrangement. Scattering was measured using either a SPEX 1403 0.85 m double monochrometer with 1200 or 2400 gr/mm holographic gratings and equipped with a thermoelectrically-cooled Burle 31034-02 GaAs photomultiplier tube and SPEX digital photometer system, or a SPEX Model 1877 CP triple monochrometer with 1200, 1800, and 2400 gr/mm holographic gratings equipped with a Princeton Instruments back-illuminated CCD detector. Scattering resolution was ~1.0 cm^{-1} at all excitation energies. Anaerobic powdered sample diluted with KBr was spun in a sealed NMR tube cooled to ~120 K (±20 K) using a nitrogen gas flow system. Profile intensities of Raman scattering peaks were determined by integration of background-corrected spectra and quantified relative to the 983.6 cm^{-1} scattering peak of solid K_2SO_4, dispersed isotropically in the NMR tube. Depolarization ratios were measured at room temperature from an anaerobic CH_3CN solution of the sample using the identical optical configuration. A normal coordinate analysis using the Wilson GF-matrix method[17] was performed with a modified version of Schachtschneider's GMAT and FPERT programs.[18,19]

Electronic Structure Calculations. Electronic structure calculations were performed using the 1982 QCPE SCF−Xα−SW programs[20] on an idealized D_{3h} structure with bond lengths and angles taken from EXAFS and crystal structure results.[11,12,14] The tridentate tmtacn ligands were approximated by three amine ligands resulting in the computational model $[Fe_2(OH)_3(NH_3)_6]^{2+}$. Details of the calculation are given elsewhere.[14] The geometries used in the $(\Delta E^{X\alpha}_{\sigma\to\sigma^*}/\Delta Q)_0$ calculations involve ±0.1 bohr (±0.05292 Å) changes in Fe···Fe internuclear separation along the $a_1'(1)$ and $a_1'(2)$ normal coordinates (*vide infra*).

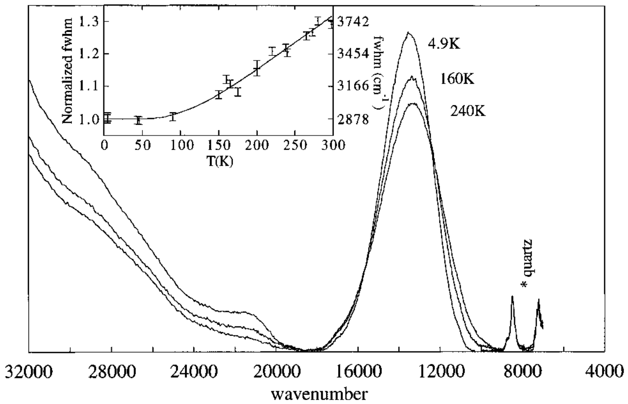

Figure 1. Variable-temperature absorption spectra of $[Fe_2(OH)_3(tmtacn)_2]^{2+}$ dissolved in 50:50 propionitrile:butyronitrile for temperatures of 4.9, 160, and 240 K. Inset: Plot of full-width half-maximum values measured at a series of temperatures. The solid line represents the least-squares best fit of the data by eq 6 and yields $\nu_{eff} = 273$ cm^{-1}.

Results

Electronic Absorption. In Figure 1, representative spectra are presented showing the variable-temperature behavior of the absorption spectrum of $[Fe_2(OH)_3(tmtacn)_2]^{2+}$ in a 50:50 propionitrile:butyronitrile solvent matrix. A linear baseline has been subtracted to compensate for differences in background absorption between frozen glass (4.9 K) and solution (160, 240 K) spectra. As the temperature is increased from 4.9 to 240 K the intense near-IR feature is observed to broaden asymmetrically, gaining significant intensity to the lower energy side while not changing significantly at the high energy side. The peak maximum of the near-IR band is also observed to shift slightly to lower energy and decrease in intensity as the temperature is increased. The integrated intensity, however, is constant to within ~4% throughout the temperature range. Plotted in the inset of Figure 1 is the temperature-dependence of the near-IR peak's full width at half max (fwhm) for a larger set of temperatures. The absorption feature at 21 500 cm^{-1} is also temperature dependent, having a maximum peak intensity at low temperature. The two sharp features at ~8000 cm^{-1} are due to quartz absorption from the cryostat and sample-cell windows.

Raman. The ~120 K solid-state preresonance Raman scattering spectrum of $[Fe_2(OH)_3(tmtacn)_2]^{2+}$ obtained with 647 nm excitation is shown in Figure 2. Observable are four low-frequency fundamental bands (Table 1) and several higher-frequency combination and overtone bands. Figure 2 (inset) compares the 568 nm preresonance Raman spectra of $[Fe_2(^{16}OH)_3(tmtacn)_2]^{2+}$ and $[Fe_2(^{18}OH)_3(tmtacn)_2]^{2+}$. All observed fundamental, combination, and overtone bands shift to lower energy upon ^{18}O substitution, and the shifts of the fundamental bands are listed in Table 1.[21]

Low-temperature solid-state Raman spectra were obtained at a series of excitation energies between 24 600 and 12 500 cm^{-1},

---

(14) Gamelin, D. R.; Bominaar, E. L.; Kirk, M. L.; Wieghardt, K.; Solomon, E. I. *J. Am. Chem. Soc.*, in press.

(15) Hush, N. S. *Prog. Inorg. Chem.* **1967**, *8*, 391−444.

(16) See for example: Marcus, R. A.; Sutin, N. *Biochim. Biophys. Acta* **1985**, *811*, 265−322.

(17) Wilson, E. B., Jr.; Decius, J. C.; Cross, P. C. *Molecular Vibrations;* Dover Edition; Dover Publications, Inc.: New York, 1980.

(18) Schachtschneider, J. H. Technical Report Nos. 231-264 and 57-65; Shell Development Co.: Emeryville, CA, 1964−1965.

(19) Fuhrer, H.; Kartha, V. B.; Kidd, K. G.; Krueger, P. J.; Mantsch, H. H. *NRCC Bulletin No. 15*; National Research Council Canada: Ottawa, 1976.

(20) Cook, M.; Case, D. A. *QCPE Program 465* **1991**, *23*, 21−22.

(21) Although far-IR spectra of the ^{16}O and ^{18}O isotopomers show several bands in the region between 120 and 600 cm^{-1}, no measurable isotopic sensitivity could be reliably identified. Two bands are observed in the ^{16}O spectrum at 361 and 285 cm^{-1} that have no counterparts in the ^{18}O spectrum, while all other bands observed remain unshifted between the isotopomers.

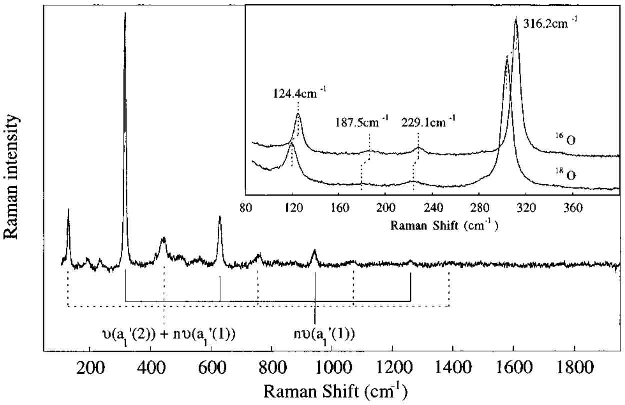

Figure 2. ~120 K solid-state resonance Raman spectrum of $[Fe_2(OH)_3(tmtacn)_2]^{2+}$ using 676 nm excitation. Two progressions involving a series of overtones in the 316 cm^{-1} mode are indicated. Inset: ~120 K solid-state isotopic shifts of the fundamental Raman scattering peaks observed with 568 nm excitation.

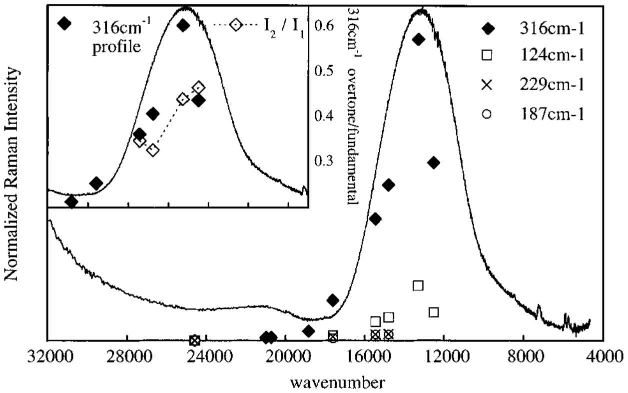

Figure 3. ~120 K solid-state resonance Raman excitation profiles for the four fundamental bands observed at 316, 229, 187, and 124 cm^{-1}. Superimposed is the 8 K solid-state absorption spectrum. Inset: ~120 K solid-state resonance Raman excitation profile for the 316 cm^{-1} mode compared with the excitation dispersion of the overtone-to-fundamental intensity ratio. Superimposed is the 8 K solid-state absorption spectrum.

Table 1. Summary of Vibrational Raman Results

band assignments	^{16}O (obs), cm^{-1}	^{18}O (obs), cm^{-1}	ρ(568 nm)	ρ(752 nm)	rel integrated intens (av)
$a_1'(1)$	316.2	308.5	0.35 ± 0.04	0.36 ± 0.04	6.6 ± 0.8
$e''(6)$	229.1	224.1			(0.3)
$e'(4)$	187.5	180.8	0.25 ± 0.07		(0.3)
$a_1'(2)$	124.4	119.8	0.35 ± 0.05	0.38 ± 0.03	1.0

all lines giving similar spectra. The ~120 K solid-state Raman intensities of the four observed fundamental bands relative to the 983.6 cm^{-1} scattering peak of K_2SO_4 are plotted in Figure 3 as a function of excitation energy and related to the 8 K solid-state absorption spectrum. The error bars on these same data shown in Figure 6b represent estimated uncertainties in relative intensities between excitation wavelengths and include contributions from temperature and standard-intensity measurements. Raman enhancement is dominated by 316 and 124 cm^{-1} scattering peaks, which are seen to gain intensity under the large absorption feature at ~13 500 cm^{-1} and have maximum resonant intensity at the absorption maximum. There is no discernible intensity enhancement under the ~21 000 cm^{-1} absorption feature and virtually no observable intensity at 24 585 cm^{-1}, the highest energy data point. Room-temperature CH_3CN solution spectra of $[Fe_2(OH)_3(tmtacn)_2]^{2+}$ (data not shown) give essentially identical vibrational spectra and resonance Raman excitation profiles as in the solid state. Solution depolarization ratios at preresonance and/or resonance excitation energies for the 316, 124, and 229 cm^{-1} bands are reported in Table 1. Figure 3 (inset) shows the ratio of first-overtone (~631 cm^{-1}) to fundamental intensities in the 316 cm^{-1} mode as a function of excitation energy through resonance, and relates this to the 316 cm^{-1} fundamental excitation profile and the 8 K solid state absorption spectrum. The overtone-to-fundamental intensity ratio does not have its maximum corresponding to the fundamental enhancement maximum but is asymmetric with greater values to lower energy. No overtone in the 124 cm^{-1} mode was observable.

Analysis. (A) Vibrational Normal Coordinates. $[Fe_2(OH)_3(tmtacn)_2]^{2+}$ has $(3N - 6) = 27$ metal–ligand vibrational degrees of freedom. In the limit of no coupling between bridging and terminal motions only the 9 metal–ligand vibrational degrees of freedom of the $[Fe_2(OH)_3]^{2+}$ core contribute to ^{18}O-sensitive vibrations. In D_{3h} symmetry these core internal coordinates combine to generate two a_1' (Raman), one a_2'' (IR), two e' (IR, Raman), and one e'' (Raman) normal modes of vibration. In the preresonance and resonance Raman spectra of $[Fe_2(OH)_3(tmtacn)_2]^{2+}$ four fundamental vibrations are observed at 124.4, 187.5, 229.1, and 316.2 cm^{-1} (±1.0 cm^{-1}, Figure 2 (inset) and Table 1), and these serve as origins for four progressions, each based on increasing quanta of the 316 cm^{-1} mode (Figure 2). These vibrations are all ^{18}O sensitive with no shifts smaller than ~4.5 cm^{-1} (Figure 2 (inset) and Table 1), reflecting large contributions from bridging OH in all observed modes.

The two strongest fundamental Raman bands (316 and 124 cm^{-1}) are both polarized in preresonance (Table 1) and are assigned as the totally-symmetric in-phase "breathing" ($a_1'(1)$) and out-of-phase "accordion" ($a_1'(2)$) modes of the $[Fe_2(OH)_3]^{2+}$ core, respectively, consistent with previous vibrational studies of isostructural M_2L_9-type compounds.[22–25] The weak bands observed at 187 and 229 cm^{-1} are assigned on the basis of NCA calculations (*vide infra*) and previous studies as the nontotally-symmetric $e'(4)$ and $e''(6)$ $[Fe_2(OH)_3]^{2+}$ core modes, which gain limited resonance Raman intensity through low-symmetry effects. Noteworthy is the absence of any fundamental or even-harmonic series of overtones attributable to the $a_2''(Q_-)$ symmetry-breaking mode anticipated to be active in mixed-valence dimers.[5]

Normal-coordinate calculations using the vibrational energies and assignments of the ^{16}O- and ^{18}O-isotopomers have been performed on an approximate $Fe(O')_3Fe$ five-body core using D_{3h}-idealized bond lengths and angles (Fe···Fe 2.509 Å, Fe–OH 1.944 Å, Fe–O–Fe 80.38°, O–Fe–O 82.84°) adapted from EXAFS and crystal-structure results.[11,12,14] The masses of the bridges were taken to be 17 g/mol, equal to that of the entire OH unit,[26] the metal atoms were used at atomic mass, 56 g/mol, and coupling of the ancillary ligand vibrations to those of the $[Fe_2(OH)_3]^{2+}$ core was neglected on the basis of the observed isotopic shifts to simplify the calculation. The general-valence F-matrix for the five-atom core was symmetrized by a D_{3h} U-matrix, allowing vibrational assignments based on group

---

(22) Durig, J. R.; Omura, Y.; Mercer, E. E. *J. Mol. Struct.* **1975**, *29*, 53–63.

(23) Black, J. D.; Dunsmuir, J. T. R.; Forrest, I. W.; Lane, A. P. *Inorg. Chem.* **1975**, *14*, 1257–1262.

(24) Ziegler, R. J.; Risen, W. M., Jr. *Inorg. Chem.* **1972**, *11*, 2796–2803.

(25) Beattie, I. R.; Gilson, T. R.; Ozin, G. A. *J. Chem. Soc. A* **1968**, 2765–2771.

(26) Little coupling is expected between the motions of the hydroxide proton and the Fe_2O_3 core due to the large energy differences between these motions. For example, the CuOH bend in $Cu_2(OH)_2$ occurs at ~950 cm^{-1}, which is significantly greater than the ^{18}O-sensitive vibrational energies seen in Figure 2: Ferraro, J. R.; Walker, W. R. *Inorg. Chem.* **1965,** *4*, 1382.

Table 2. Results from the General Valence Normal Coordinate Vibrational Analysis on the Five-Atom Fe(O′)$_3$Fe Core[a]

Vibrational Energies (cm^{-1}) for Normal Modes (*n*)

	a$_1$′(1)	a$_1$′(2)	a$_2$″(3)	e′(4)	e′(5)	e″(6)
^{16}O obs (^{18}O obs)	316.2 (308.5)	124.4 (119.8)		187.5 (180.8)		229.1 (224.1)
^{16}O calc (^{18}O calc)	316.2 (309.0)	124.4 (120.4)	306.1 (294.9)	187.8 (180.9)	96.7 (91.4)	231.5 (222.1)

Normal Coordinate Descriptions

internal coords (*i*)	F_{ii}	L_1	PED	L_2	PED	L_3	PED	L_4	PED	L_5	PED	L_6	PED
(1) Fe···Fe		0.1424		0.1246		0.0000		0.0000		0.0000		0.0000	
(2) Fe−OH	0.560	0.1164	100.0	−0.0403	22.1	±0.1091	73.9	−0.1154	83.7	−0.0882	58.0	±0.1271	91.8
(3) Fe−O−Fe	0.186	−0.0052	0.0	0.1189	31.9	0.0000	0.0	0.1003	10.4	0.0766	7.3	0.0000	0.0
(4) O−Fe−O	0.241	0.0039	0.0	−0.0886	46.0	±0.0990	26.1	0.0467	5.9	−0.1040	34.7	±0.0577	8.2

[a] Observed and calculated vibrational energies for each normal mode (*n*), internal coordinate (*i*) definitions, principal force constants (F_{ii}, mdyn/Å), eigenvectors ($L_n = (l_{1n}, l_{2n}, ...)$), and potential-energy distributions (PEDs). Only one component of each degenerate mode is reported. PEDs are reported as the normalized contributions of each principal force constant to the normal mode, *n*: $[(F_{ii}l_{in}^2/\sum_i F_{ii}l_{in}^2) \times 100]$.

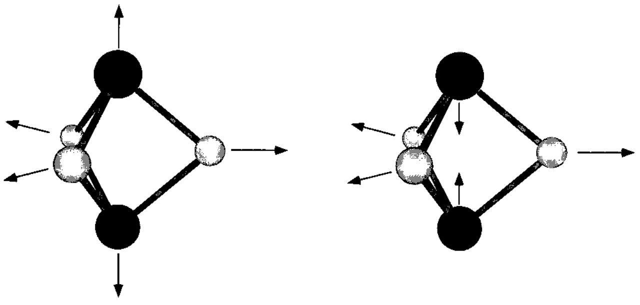
a$_1$′(1): 316cm^{-1} a$_1$′(2): 124cm^{-1}

Figure 4. Depiction of the a$_1$′(1) and a$_1$′(2) vibrational normal mode descriptions obtained from the normal-coordinate analysis of [Fe$_2$(OH)$_3$(tmtacn)$_2$]$^{2+}$ based on the Raman vibrational data of Figure 2. The arrows shown are scaled to represent relative nuclear displacements from the molecular origin in the +a$_1$′(1) and −a$_1$′(2) phases.

theory and spectroscopic selection rules to be used in the calculations. For the purpose of mode description, an additional Fe···Fe internal coordinate was included throughout the calculation, with all related restoring and interaction force constants held at zero to avoid additional closed-ring redundancies. Due to the existing closed-ring redundancies of the Fe(O′)$_3$Fe core any contribution from the neglected Fe···Fe restoring force, which is expected to be small based on the Fe···Fe distance and the low energy of the a$_1$′(t$_{2g}$) → a$_2$″(t$_{2g}$) $\sigma \rightarrow \sigma^*$ transition,[27] will be accommodated by other force constants (principally that of the Fe−(OH)−Fe bend) but will not significantly affect the eigenvector descriptions of the normal modes.[28] Table 2 lists the observed and calculated frequencies (ν (cm^{-1})), principal force constants (F_{ii}), eigenvectors (*L*), and potential-energy distributions (PEDs) among the principal force constants from the general-valence normal-coordinate analysis based on the vibrational data in Figure 2. The complete force-field parameter set is provided as Supporting Information.

Descriptions of the two a$_1$′ vibrational modes obtained from the NCA calculation are presented pictorially in Figure 4. The eigenvectors and potential-energy distributions for these two modes indicate that the 316 cm^{-1} vibration (a$_1$′(1)) is described as primarily Fe−OH stretching, while the 124 cm^{-1} band (a$_1$′(2)) involves large contributions from both stretch and bend internal coordinates and thus occurs at lower energy. Similarly, the two e′ modes involve mixing of the stretch and bend e′ symmetry coordinates, while the a$_2$″ and e″ stretching modes are restricted by symmetry to have no contribution from the Fe−O−Fe bending coordinates. Note that only the two a$_1$′ modes are of appropriate symmetry to involve any variation in Fe···Fe internuclear separation. The ordering of the e′(4) and e″(6) band assignments as the 187 and 229 cm^{-1} vibrations, respectively, is based on this calculation, as reversal of these assignments leads to nonphysical results manifested by negative eigenvalues for the lowest-energy e′(5) vibration (not observed). The precise frequencies of the e′(5) and a$_2$″ vibrations and the ordering of the e′(4) and e″(6) vibrations, however, have little effect on the calculated eigenvectors of the two a$_1$′ vibrations. In summary, the normal-mode descriptions for the two dominant vibrations observed in the resonance Raman spectra of [Fe$_2$(OH)$_3$(tmtacn)$_2$]$^{2+}$ have been calculated from the Raman vibrational data of Figure 2. These two modes are seen to involve stretch and bend motions of the [Fe$_2$(OH)$_3$]$^{2+}$ core, and in particular, both involve motion along the Fe···Fe internuclear coordinate. For use in further analysis, the positive phases of the a$_1$′(1) and a$_1$′(2) coordinates are defined to coincide with increasing Fe···Fe separation (Table 3).

(B) $\sigma \rightarrow \sigma^*$ Excited-State Distortion Analysis Using Harmonic-Potential Approximations. (i) Resonance Raman Intensities. The two totally-symmetric core vibrational modes of [Fe$_2$(OH)$_3$(tmtacn)$_2$]$^{2+}$ (Figure 4) both show large resonance Raman intensity enhancement when excitation is in resonance with the near-IR a$_1$′(t$_{2g}$) → a$_2$″(t$_{2g}$) transition (Figure 3). This observation indicates that a significant geometric distortion occurs along both normal coordinates upon excitation. Quantitative excited-state distortion parameters can be obtained from resonance Raman data using the approximate expression developed by Warshel[29,30] and by Blazej and Peticolas[31] (eq 1), which emphasizes the relationship between preresonance (or

$$I_n \propto \left| \frac{\Delta_n \nu_n}{(E_0 + i\Gamma)(E_0 - \nu_n + i\Gamma)} \right|^2 \qquad (1)$$

short time-scale) Raman intensities, I_n, vibrational energies, ν_n (cm^{-1}), and dimensionless excited-state potential displacements, Δ_n,[32] where E_0 (cm^{-1}) is the excitation detuning interval, $E_0 = E_{ex} - E_{0-0}$, and Γ is a damping factor. The dimensionless normal-coordinate displacement parameter, Δ_n, is related to the

---

(27) $\sigma \rightarrow \sigma^*$ energies for other transition-metal dimers: Abrahamson, H. B.; Frazier, C. C.; Ginley, D. S.; Gray, H. B.; Lilienthal, J.; Tyler, D. R.; Wrighton, M. S. *Inorg. Chem.* **1977**, *16*, 1554−1556.

(28) Bulliner, P. A.; Spiro, T. G. *Spectrochim. Acta* **1970**, *26A*, 1641−1650.

(29) Warshel, A. *Annu. Rev. Biophys. Bioeng.* **1977**, *6*, 273−300.

(30) Warshel, A.; Dauber, P. *J. Chem. Phys.* **1977**, *66*, 5477−5488.

(31) Blazej, D. C.; Peticolas, W. L. *Proc. Natl. Acad. Sci. U.S.A.* **1977**, *74*, 2639−2643.

(32) See also: Myers, A. B.; Mathies, R. A. In *Biological Applications of Raman Spectroscopy*; Spiro, T. G., Ed.; Wiley: New York, 1987; Vol. 2, pp 1−58.

Table 3. Equilibrium Geometry of $[Fe_2(OH)_3(tmtacn)_2]^{2+}$ in the $\sigma \rightarrow \sigma^*$ Excited State, Derived from Approximate Harmonic Analysis of the Variable-Temperature Absorption and Resonance Raman Excitation Profile Data

	int coord displacements, Δr^a		possible excited-state distortions from harmonic approximations			
int coord	+ $a_1'(1)$: 316.2 cm^{-1}	+ $a_1'(2)$: 124.4 cm^{-1}	+ +	+ −	− +	− −
Fe···Fe, Å	+0.2367	+0.3302	0.567	−0.093	0.093	−0.567
Fe−OH, Å	+0.1935	−0.1068	0.087	0.301	−0.301	−0.087
Fe−O−Fe	−0.0086	+0.3151	0.306	−0.323	0.323	−0.306
O−Fe−O	+0.0065	−0.2348	−0.228	0.242	−0.242	0.228
Displacement from Origin with Excitation (Å)						
Fe			0.284	−0.047	0.047	−0.284
O			−0.159	0.418	−0.418	0.159
(ratio Fe:O)			(+1.79:−1)	(−1:+8.89)	(+1:−8.89)	(−1.79:+1)

[a] Calculated from eq 7 and the normal mode descriptions of Table 2 using $|\Delta_1| = |\Delta_2| = 5.09$.

dimensioned parameter ΔQ_n(Å) by eq 2, where the scaling

$$\Delta Q_n = \delta \Delta_n = \frac{5.8065}{\sqrt{\mu_n \nu_n}} \Delta_n \qquad (2)$$

factor, δ, is defined as

$$\delta \equiv \sqrt{\frac{\nu_n}{k_n}}$$

for a modal force constant of $k_n = 4\pi^2 c^2 m_n \nu_n^2$ (expressed in units of $(cm^{-1}/Å^2)^{33}$). m_n is the modal reduced mass

$$m_n = \frac{\mu_n}{N_A}$$

where μ_n is the molar reduced mass for normal mode Q_n in grams per mole and N_A is Avagadro's number. The derivation of eq 1 involves the simplifying approximations of equal ground- and excited-state harmonic potential parameters, identical ground- and excited-state normal-coordinate descriptions (*i.e.* no Duschinsky rotation[34]), small potential shifts, and low temperatures ($kT \ll \nu$ (cm^{-1})).

From eq 1, the relative intensities of two modes, *m* and *n*, in a preresonance (E_0 large) Raman spectrum are then related to the relative coordinate displacements by the expression

$$\frac{I_n}{I_m} \approx \frac{\Delta_n^{\,2} \nu_n^{\,2}}{\Delta_m^{\,2} \nu_m^{\,2}} = \frac{(\Delta Q_n)^2 \mu_n \nu_n^{\,3}}{(\Delta Q_m)^2 \mu_m \nu_m^{\,3}} \qquad (3)$$

Using eq 3 and the ~120 K relative a_1' fundamental Raman scattering intensities ($I_{a_1'(1)}/I_{a_1'(2)} \approx 6.6$, Table 1), the relative dimensionless displacement along the $a_1'(1)$ (316 cm^{-1}) and $a_1'(2)$ (124 cm^{-1}) normal coordinates accompanying the $a_1'(t_{2g}) \rightarrow a_2''(t_{2g})$ electronic excitation is approximately $|\Delta_{a_1'(1)}/\Delta_{a_1'(2)}| = 1.0 \pm 0.1$. The role of vibrational frequency in determining the observed resonance Raman scattering intensity is particularly apparent in this system, and this observation emphasizes the need to include analysis of low-intensity vibrations in studies of excited-state distortions if their frequencies are low, as is often the case with metal−ligand vibrations.

Absolute scaling of these relative displacement parameters, Δ, can be obtained from the LT-absorption spectrum with the additional assumption that the absorption bandwidth arises exclusively from Franck−Condon progressions in these two vibrational coordinates[35] such that

$$\text{fwhm} \approx [4 \ln 2 \sum_k \Delta_k^{\,2} \nu_k^{\,2}]^{1/2} \qquad (4)$$

For equal excited-state displacements in the 316 and 124 cm^{-1} modes (*i.e.* $|\Delta_1| = |\Delta_2| = |\Delta|$), the LT-absorption bandwidth (2880 cm^{-1}, Figure 1) and eq 4 give $|\Delta| = 5.09$. These dimensionless normal-coordinate displacements can be related to the Huang−Rhys harmonic displacement parameter[35,36]

$$S_i = \frac{E_{R(i)}}{\nu_i} = \frac{{}^1\!/_2 k_i (\Delta Q_i)^2}{\nu_i} = \frac{\Delta_i^{\,2}}{2} \qquad (5)$$

yielding $S = 13$ (where $S_1 = S_2 = S$), and excited-state vibrational-relaxation energies, $E_{R(i)} = {}^1\!/_2 k_i (\Delta Q_i)^2$, of $E_{R(1)} = 4100$ cm^{-1} and $E_{R(2)} = 1610$ cm^{-1}.

(ii) Variable-Temperature Absorption. The excited-state displacement may alternatively be quantified in the harmonic approximation by moment analysis of the absorption bandwidth. The temperature dependence of the absorption bandwidth, shown in Figure 1 (inset), is fit to the second-moment hyperbolic cotangent function:[35]

$$\frac{\text{fwhm}(T)}{\text{fwhm}(T_0)} = \sqrt{\coth\left(\frac{\nu_{\text{eff}}}{2kT}\right)} \qquad (6)$$

From this analysis an effective vibronic mode frequency of $\nu_{\text{eff}} = 273$ cm^{-1} is obtained, which can be used to deduce the effective dimensionless displacement using eq 4. This gives $|\Delta_{\text{eff}}| = 6.32$, and a total excited-state vibrational-relaxation energy of $E_{R(\text{eff})} = 5450$ cm^{-1} (eq 5), compared to the value obtained from the use of the actual vibrational frequencies of $E_{R(1)} + E_{R(2)} = 5710$ cm^{-1}.

(iii) Excited-State Equilibrium Geometry. The excited-state distortion resulting from the $a_1'(t_{2g}) \rightarrow a_2''(t_{2g})$ transition in $[Fe_2(OH)_3(tmtacn)_2]^{2+}$ may then be expressed in terms of internal coordinates using the calculated coordinate descriptions from the normal-coordinate analysis (*vide supra*) and eq 2. The dimensioned distortion parameters for the two a_1' modes are $|\Delta Q_1| = 0.434$ Å and $|\Delta Q_2| = 0.534$ Å, computed using modal masses of $\mu_1 = 14.6$ g/mol and $\mu_2 = 24.6$ g/mol derived by rediagonalization of the NCA G-matrix symmetrized along the normal coordinates. These give a ratio of $|\Delta Q_{a_1'(1)}/\Delta Q_{a_1'(2)}| \approx 0.81$. As the sign of the displacement, ΔQ, is ambiguous in the harmonic treatment, there are four possible phase combinations (+ +, + −, − +, − −) of $a_1'(1)$ and $a_1'(2)$ coordinate displacements in this excited state. The internal-coordinate

---

(33) k_n/hc gives units of $cm^{-1}/Å^2$.
(34) Duschinsky, F. *Acta. Physicochem. URSS* **1973**, 551.
(35) Solomon, E. I. *Comments Inorg. Chem.* **1984**, *3*, 227−320.
(36) Huang, K.; Rhys, A. *Proc. R. Soc. London, A* **1951**, *208*, 352.

displacements, Δr_i (Å), are determined from the normal-coordinate displacements by

$$\Delta r_i(\text{Å}) = \sum_n \left(l_{n,i}\sqrt{\mu_n}\right)\Delta Q_n = 5.8065\sum_n l_{n,i}\frac{\Delta_n}{\sqrt{\nu_n}} \qquad (7)$$

where $l_{n,i}$ is the ith element of the mass-weighted eigenvector, L_n, for the nth normal mode[32,37] (Table 2). The internal coordinate displacements, Δr (Å), are given in Table 3 for each of the two a_1' normal coordinates and for the four possible combinations of phases.

Further insight into the $a_1'(t_{2g}) \rightarrow a_2''(t_{2g})$ excited-state distortion in $[Fe_2(OH)_3(tmtacn)_2]^{2+}$ system is obtained by comparison of the fundamental and overtone Raman scattering intensities for the 316 cm^{-1} $a_1'(1)$ mode. Using the time-dependent description of resonance Raman intensities,[38,39] Morris and Woodruff have described how a change in modal force constant upon electronic excitation may manifest itself as an asymmetry of the overtone excitation profile for that mode.[40] The nature of the asymmetry reflects directly the sign of the force-constant change (Δk_{ex-gr}), thereby allowing the direction of excited-state distortion along that normal coordinate to be determined if the directions of geometric distortion and force-constant change are assumed to coincide (*i.e.* are consistent with a Badger-type rule[41,42]). From Figure 3 (inset), an asymmetric $a_1'(1)$ overtone-to-fundamental intensity profile is observed, with a positive slope from high to low energy through the absorption maximum. As described in ref 40, this yields a decreased $a_1'(1)$ modal force constant in the $\sigma \rightarrow \sigma^*$ excited state, and hence a positive (increasing Fe−OH internuclear separation) excited-state distortion, since the PED of this mode is 100% Fe−OH stretch (Table 2). Although other factors such as a nonconstant transition dipole moment (*i.e.* breakdown of the Condon approximation) may affect the shape of the overtone-to-fundamental ratio's dispersion,[43] the $a_1'(1)$ force-constant change is anticipated to dominate this behavior in $[Fe_2(OH)_3(tmtacn)_2]^{2+}$ due to the large excited-state $a_1'(1)$ coordinate displacement determined for this system. No overtone for the 124 cm^{-1} mode is reliably observed, precluding a similar analysis of the sign of distortion along the $a_1'(2)$ normal coordinate. Thus, at this level of analysis the nuclear distortion in the $a_1'(t_{2g}) \rightarrow a_2''(t_{2g})$ excited state of $[Fe_2(OH)_3(tmtacn)_2]^{2+}$ is determined to be either the + + or + − combination of $a_1'(1)$ and $a_1'(2)$ normal-coordinate displacements given in Table 3.

Table 4. SCF−Xα−SW-Calculated Changes in Transition-State Energies for Perturbed Geometries along the $a_1'(1)$ and $a_1'(2)$ Normal Coordinates and Experimental $(\partial V_{ex}^{exp}/\partial Q)_0$ Values along These Coordinates Obtained from L−J Analysis of the Variable-Temperature Absorption and Resonance Raman Profiles of $[Fe_2(OH)_3(tmtacn)_2]^{2+}$

	SCF−Xα−SW			L−J spectral analysis
Q_n	$\Delta E_{\sigma\rightarrow\sigma^*}$, cm^{-1}	ΔQ,[a] Å	$(\Delta E^{X\alpha}_{\sigma\rightarrow\sigma^*}/\Delta Q)_0$, cm^{-1}/Å	$(\partial V_{ex}^{exp}/\partial Q)_0$, cm^{-1}/Å
$a_1'(1)$ (+)	−1240	+0.0973	−13710	−17382
(−)	1430	−0.0973		
$a_1'(2)$ (+)	−2790	+0.0856	−30671	−7974[b]
(−)	2460	−0.0856		

[a] All ±ΔQs correspond to changes of ±0.05292 Å (0.1 Bohr) in the Fe···Fe separation from the equilibrium value of 2.509 Å. [b] Sign determined by Xα−SW.

(iv) Xα−SW Determination of the $\sigma \rightarrow \sigma^*$ Excited-State Distortion Direction. The directions of the $a_1'(t_{2g}) \rightarrow a_2''(t_{2g})$ excited-state distortions can be obtained from the Xα−SW description of the changes in bonding involved in this excitation. Xα−SW calculates an energy for this transition that closely matches the experimental energy (13 300 cm^{-1} (Xα−SW) vs 13 500 cm^{-1} (experimental)[14]), suggesting that the bonding changes involved in this excitation are modeled well in the calculation. These differences in bonding yield displaced excited-state potential surfaces along specific group-theoretically-allowed nuclear-distortion coordinates and result in a geometry dependence of the $a_1'(t_{2g}) \rightarrow a_2''(t_{2g})$ transition energy along these coordinates. This geometry dependence can be described to first order as a linear electron-nuclear coupling term in the excited state[35]

$$(\partial V_{ex}/\partial Q)_0 \equiv \langle \psi_{ex}|(\partial \hat{V}_{ex}/\partial Q)_0|\psi_{ex}\rangle$$

where the subscript 0 denotes the ground-state equilibrium geometry. These distortions are probed by calculation of Xα−SW $\sigma \rightarrow \sigma^*$ transition-state energies, $E^{X\alpha}_{\sigma\rightarrow\sigma^*}$, for a series of geometries perturbed by an amount ΔQ in both directions from the equilibrium geometry along each of the two a_1' normal coordinates (known from resonance Raman to dominate the excited-state distortions). These calculations provide a value for $(\Delta E^{X\alpha}_{\sigma\rightarrow\sigma^*}/\Delta Q)_0$, which equals $(\partial V_{ex}/\partial Q)_0$ in the limit of small geometric perturbations if the Xα−SW ground-state potential is at a minimum in the experimental equilibrium geometry. The large excited-state coordinate displacements along both a_1' core normal coordinates determined by the harmonic analysis above indicate that $(\partial V_{ex}/\partial Q)_0$ in the $\sigma \rightarrow \sigma^*$ excited state is large along these two coordinates, and the $(\partial V_{ex}/\partial Q)_0$ terms resulting from these coordinate displacements are therefore expected to dominate the Xα−SW $(\Delta E^{X\alpha}_{\sigma\rightarrow\sigma^*}/\Delta Q)_0$ calculations. These calculations yield large $(\Delta E^{X\alpha}_{\sigma\rightarrow\sigma^*}/\Delta Q)_0$ values along both a_1' core normal coordinates (Table 4), as seen experimentally. From Table 4, excited-state distortions involving an increase in Fe···Fe and Fe−OH internuclear separations along the $a_1'(1)$ normal coordinate result in reduced transition energies (*i.e.* $(\Delta E^{X\alpha}_{\sigma\rightarrow\sigma^*}/\Delta Q_1)_0 < 0$), consistent with the experimental direction of excited-state distortion along this coordinate obtained from analysis of the $a_1'(1)$ resonance Raman overtone intensities. Displacement along the $a_1'(2)$ normal coordinate yields a reduction in transition energy coinciding with elongation of the Fe···Fe internuclear separation and contraction along the Fe−OH internal coordinate (*i.e.* $(\Delta E^{X\alpha}_{\sigma\rightarrow\sigma^*}/\Delta Q_2)_0 < 0$). The calculation therefore determines the excited-state distortion phase to be the + + combination listed in Table 3. This combination involves a constructive combination of the two displaced normal coordinates with respect to elongation along the Fe···Fe internal coordinate, while distortions along the Fe−OH internal coordinate are oppositely signed in the two displaced coordinates and largely cancel one another.

(C) $\sigma \rightarrow \sigma^*$ Excited-State Distortion Analysis Using Anharmonic Potentials. (i) Problems with the Harmonic Approximations. Two aspects of the near-IR absorption feature (Figure 1) are not addressed in the above analysis: its asymmetric low-temperature bandshape and its asymmetric

---

(37) Wright, P. G.; Stein, P.; Spiro, T. G. *J. Am. Chem. Soc.* **1978**, *101*, 3531−3535.

(38) Heller, E. J. *Acc. Chem. Res.* **1981**, *14*, 368−375.

(39) Heller, E. J.; Sundberg, R. L.; Tannor, D. *J. Phys. Chem.* **1982**, *86*, 1822−1833.

(40) Morris, D. E.; Woodruff, W. H. *J. Phys. Chem.* **1985**, *89*, 5795−5798.

(41) Badger, R. M. *J. Chem. Phys.* **1934**, *2*, 128−131.

(42) Miskowski, V. M.; Dallinger, R. F.; Christoph, G. G.; Morris, D. E.; Spies, G. H.; Woodruff, W. H. *Inorg. Chem.* **1987**, *26*, 2127−2132.

(43) Ling, S.; Imre, D. G.; Heller, E. J. *J. Phys. Chem.* **1989**, *93*, 7107−7119.

broadening at elevated temperatures. In the harmonic theory, a small potential displacement will result in a Poisson distribution of low-temperature absorption intensity, leading to an asymmetric bandshape with a tail extending toward high energy.[35] This asymmetry arises from the sharp intensity cutoff on the low-energy side of the band that results from sizable 0−0 overlap. In the case of large distortion, where the 0−0 overlap is no longer significant, harmonic potentials give rise to an approximately Gaussian low-temperature absorption profile and additionally to symmetric broadening with increasing temperature. The $a_1'(t_{2g}) \rightarrow a_2''(t_{2g})$ transition in $[Fe_2(OH)_3(tmtacn)_2]^{2+}$ is seen from the above analysis to involve large ($S \approx 13$) excited-state potential displacements along two totally-symmetric normal coordinates, and this excitation should therefore display a fairly symmetric low-temperature absorption profile and nearly-symmetric temperature broadening were the potentials harmonic, in contrast with the experimental behavior observed in Figure 1. Attempts to simulate the near-IR absorption bandshape and temperature dependence using harmonic ground- and excited-state potentials were unsuccessful due to the inability to account for the high-energy tail. The lack of any resonance Raman enhancement involving the nontotally-symmetric a_2'' vibration (Q_- in the PKS model for vibronic coupling in mixed-valence dimers[4,5]) indicates that the LT asymmetry does not derive from vibronic progressions in this coordinate that could result from the large differences in potential curvature anticipated for delocalized mixed-valence dimers (see discussion). Additionally, the insignificant (<2%) thermal population of $S_T = {}^7/_2$ or higher-energy spin components of the ground state at elevated temperatures, determined by variable-temperature magnetic susceptibility experiments,[14] rules out the possibility of significant lower-energy contributions to the VT-absorption bandshapes due to electronic excitation between spin states with $S_T < {}^9/_2$. Thus, the bandshape and temperature dependence of the experimental absorption data cannot be reconciled with the large coordinate displacements determined in the harmonic analysis of Raman intensities and absorption bandwidths. To obtain a more accurate description of the bonding changes involved in the $a_1'(t_{2g}) \rightarrow a_2''(t_{2g})$ near-IR excitation of $[Fe_2(OH)_3(tmtacn)_2]^{2+}$, the model used for analysis of the variable-temperature absorption bandshapes and resonance Raman excitation profiles (RREPs) is therefore extended to account for more realistic aspects of the ground- and excited-state potential-energy surfaces, the most important modification being the inclusion of anharmonicity.[44]

(ii) Excited-State Anharmonicity Effects in Absorption Spectroscopy. The overlap integrals required for the simulation of absorption and resonance Raman data using anharmonic potentials (eq 8) are evaluated by numerical integration over

$$\langle i|v\rangle \equiv \langle \psi_i^{\mathrm{gr}}|\psi_v^{\mathrm{ex}}\rangle \tag{8}$$

individual overlap products of the numerical solutions to the Schrödinger equation derived for anharmonic ground- and excited-state potentials. The Franck−Condon (FC) factors, given by the squares of the overlap integrals, are then substituted into expressions for temperature-dependent light absorption and resonance Raman scattering intensities to generate simulated spectra. The details of this calculational approach are presented in the Appendix.

The anharmonic potentials used in the calculation are Lennard−Jones (L−J) potentials defined by

$$W_{\mathrm{gr}}(x) = 4V_0(x^{-12} - x^{-6}) \tag{9a}$$

$$W_{\mathrm{ex}}(x) = E_{0-0} + W_{\mathrm{gr}}(x - \Delta x) \tag{9b}$$

where W_{gr} and W_{ex} refer to the ground- and excited-state potentials, V_0 (cm^{-1}) is a measure of the potential's depth, E_{0-0} (cm^{-1}) is the difference in energies of the ground- and excited-state potential minima, and x is the dimensionless distance parameter associated with a particular dimensioned nuclear coordinate, Q. Representative ground- and excited-state L−J potentials calculated from eqs 9a and 9b are illustrated in Figure 5a, in which the horizontal axis is represented as $x - x_{0,\mathrm{gr}}$, where $x_{0,\mathrm{gr}}$ denotes the ground-state minimum (at $x = 2^{1/6}$). The principal objective of the spectroscopic simulations is determination of the dimensionless displacement parameters, $\Delta x_n = (x_{0,\mathrm{ex}}) - x_{0,\mathrm{gr}})_n$ (Figure 5a), that describe the magnitude of excited-state potential displacement along vibrational normal coordinates Q_n, where $Q_n = a_1'(1)$ and $a_1'(2)$ in the case of $[Fe_2(OH)_3(tmtacn)_2]^{2+}$. Δx_n is the L−J analog of the harmonic dimensionless displacement parameter, Δ_n, and is related to the dimensioned normal-coordinate displacement parameter, ΔQ_n (Å), using eq 10, where the scaling factor $a = \delta[2^{5/6}(3\gamma)]^{1/2}$ is

$$Q = ax \tag{10}$$

a measure of the potential width, $\delta \equiv [\nu_n/k_n]^{1/2}$ as in eq 2, and γ, ν_n, and k_n are defined below. As in the harmonic analysis, solution of Δx_n thus allows description of the excited-state distortions in terms of internal-coordinate changes, Δr_i (Å), using eq 7 and the NCA normal-mode descriptions of Table 2.

Solutions for Δx_n are obtained by simulation of the experimental absorption and RR data using FC overlap factors calculated for the potential surfaces given by eqs 9a and 9b as a function of Δx_n. The wavefunctions needed for calculation of the overlap integrals are solutions[45] of the Schrödinger equation for movement of an effective mass, m, along x are given in eq 11a and rewritten in dimensionless form in eq 11b

$$\left[-\frac{\hbar^2}{2ma^2}\frac{\partial^2}{\partial x^2} + W(x)\right]\psi_n = E_n\psi_n \tag{11a}$$

$$\left[-\frac{1}{\gamma^2}\frac{\partial^2}{\partial x^2} + V(x)\right]\psi_n = \epsilon_n\psi_n \tag{11b}$$

by expressing energies in units of V_0 using the following definitions:

$$\gamma = \sqrt{\frac{2ma^2V_0}{\hbar^2}} \tag{11c}$$

$$V = \frac{W}{V_0} \tag{11d}$$

$$\epsilon_n = \frac{E_n}{V_0} \tag{11e}$$

---

[44] See for example: Hollas, J. M. *Modern Spectroscopy*; John Wiley & Sons: Chichester, England, 1987; Chapter 7.

[45] Koonin, S. E.; Meredith, D. C. *Computational Physics*; Addison-Wesley Pub.: Reading, MA, 1989.

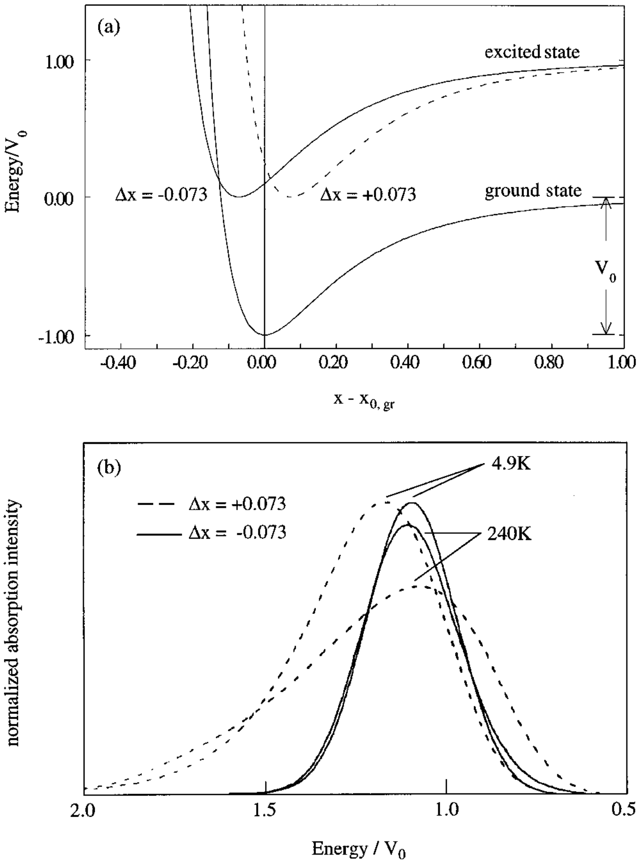

Figure 5. (a) Anharmonic potentials and selected parameters used for simulation of VT-absorption and resonance Raman data, illustrating the differences in $(\partial V_{ex}/\partial x)_0$ in the FC-overlap region between surfaces having positive ($\Delta x > 0$) and negative ($\Delta x < 0$) coordinate displacements relative to the ground-state minimum $x = x_{0,gr}$. The specific parameters used are $E_{0-0} = V_0$ and $\Delta x = \pm 0.073$. (b) Simulated variable-temperature absorption curves using these parameters and a vibrational energy of 124 cm^{-1} for temperatures of 4.9 and 240 K, normalized to the 4.9 K intensity maximum. Absorption in the positively-displaced case shows significantly greater temperature dependence due to the larger $\partial V_{ex}/\partial x$ in the FC region.

The ground- and excited-state potential functions from eqs 9a and 9b (($W_{gr}(x)$ and $W_{ex}(x)$)) are thus substituted into eq 11a for $W(x)$. Note in eq 11b that larger values of γ result in more classical descriptions of the vibrational energy associated with these potential surfaces.

In the vicinity of the potential minimum of each surface (x_0), where $(dV/dx)_{x_0} = 0$ and $V(x_0) = -1$ (energy/V_0, Figure 5a), the L−J potential is approximately the equivalent of a harmonic potential with a dimensionless force constant of $k = (d^2V/dx^2)_{x_0} = 72(2^{-1/3})$ (in units of V_0/a^2) and a $v = 0$ to $v = 1$ vibrational-quantum spacing of ν (in cm^{-1}). From the definitions of a, γ, and δ given above, the depth of the L−J well relative to ν is then

$$\frac{V_0}{\nu} = \frac{\gamma}{6(2^{5/6})} \tag{12}$$

γ is thus also a measure for the depth of the L−J potential well in units of ν.

The absorption bandshapes calculated using L−J potentials differ significantly from those calculated using harmonic potentials, particularly in cases of large coordinate displacement as found in $[Fe_2(OH)_3(tmtacn)_2]^{2+}$. In the ground state, only vibrational levels near the L−J potential minimum are populated, and these are similar to those of a harmonic surface. Differences in absorption bandshapes relative to those predicted by a harmonic analysis are therefore mainly determined by the anharmonic properties of the excited-state potential surface, making bandshape analysis a sensitive probe of the excited-state surface. These differences are attributable to two features of the anharmonic excited-state surface: the asymmetry of this surface with respect to its potential minimum and the increasing density of excited-state vibrational levels as the dissociation limit is approached. These features have the important consequence of yielding significantly different spectral properties depending on whether excited-state distortion involves a positive ($\Delta x > 0$) or negative ($\Delta x < 0$) L−J potential displacement (where a positive excited-state Δx involves displacement of this surface toward the dissociation limit, as shown in Figure 5a).

Figure 5a compares the FC overlap regions for positive and negative excited-state L−J displacements of equal magnitude. In the case of a positive displacement ($\Delta x > 0$), the slope of the excited-state potential surface around the ground-state equilibrium geometry, $(\partial V_{ex}/\partial Q)_0$, is large, resulting in FC overlap being distributed over a wide range of excited-state vibrational energy levels (Figure 5a, dashed line). In the negative displacement case ($\Delta x < 0$), $(\partial V_{ex}/\partial Q)_0$ is smaller and the FC region is hence spanned by a narrower range of excited-state vibrational energy levels (Figure 5a, solid line). For large distortions, positive displacement leads to an asymmetric low-temperature absorption profile tailing to higher energies (Figure 5b, 4.9 K dashed line), in contrast with a fairly symmetric low-temperature absorption profile resulting from a negative displacement (Figure 5b, 4.9 K solid line). Note that the directions of the temperature-dependent maximum shift and the small asymmetric tail are also reversed in Figure 5b upon changing the sign of Δx.[46] For small distortions the FC region is near the excited-state potential minimum, which is nearly harmonic, and the absorption bands obtained from excited-state displacements of equal magnitude and opposite sign are nearly identical.

Increasing the temperature to thermally populate the $v = 1$ ground-state vibrational level changes the properties of the ground-state wavefunction significantly, introducing a vibrational wavefunction having a node at $x_{0,gr}$ rather than a maximum. As a result the temperature dependence of the absorption profile is also very sensitive to $(\partial V_{ex}/\partial Q)_0$. If $(\partial V_{ex}/\partial Q)_0$ is large (*e.g.* for $\Delta x > 0$ in Figure 5a), this change in the ground state will result in a large temperature dependence of the absorption bandshape (Figure 5b, dashed line). Alternatively, a small $(\partial V_{ex}/\partial Q)_0$ (*e.g.* for $\Delta x < 0$ in Figure 5a) will result in a smaller temperature dependence of the absorption bandshape (Figure 5b, solid line).

(iii) Anharmonic Effects in the Spectroscopy of $[Fe_2(OH)_3(tmtacn)_2]^{2+}$. From the harmonic analysis presented above, the $a_1'(t_{2g}) \rightarrow a_2''(t_{2g})$ transition is found to involve large and approximately equal dimensionless displacements (Δ) along two totally-symmetric normal coordinates. The large relative difference in vibrational energies (316 vs 124 cm^{-1}) along these two coordinates allows the properties of the absorption spectrum to be roughly deconvoluted into (*i*) the low-temperature bandshape, which will be dominated by the higher-frequency mode, and (*ii*) the variable-temperature bandshape changes, which will be dominated by the temperature-dependence of the contribution from the lower-frequency mode. As the low-temperature bandshape (Figure 1) is mainly determined by the 316 cm^{-1} mode, the asymmetric tail to high energy suggests that the excited-state displacement is in the positive ($\Delta x > 0$) direction along this coordinate, consistent with the result obtained from the resonance Raman overtone excitation profile

---

[46] A recent example of bandshape asymmetry attributed to $\Delta x < 0$ in an anharmonic excited state is found in: Miskowski, V. M.; Rice, S. F.; Gray, H. B.; Dallinger, R. F.; Milder, S. J.; Hill, M. G.; Exstrom, C. L.; Mann, K. R. *Inorg. Chem.* **1994**, *33*, 2799−2807.

(Figure 3, inset) and the Xα−SW $(\Delta E^{X\alpha}_{\sigma\rightarrow\sigma^*}/\Delta Q)_0$ values (Table 4). The large intensity redistribution observed upon increasing the temperature suggests that the sign of the excited-state displacement along the $a_1'(2)$ mode is also positive, since negative distortions result in much smaller temperature dependence than is experimentally observed (Figure 5b). These observations are borne out by quantitative simulations of the resonance Raman excitation-profile (RREP) and VT-absorption data using anharmonic potentials.

The spectra of $[Fe_2(OH)_3(tmtacn)_2]^{2+}$ were initially simulated with anharmonic potentials using identical ground- and excited-state parameters along each of the two normal-coordinates by the methods outlined in the Appendix, and the relative displacements, ΔQ_1 and ΔQ_2, were constrained to the 0.81:1 ratio approximated from the Raman intensities using eq 3. Simulated absorption and resonance Raman data under these constraints using anharmonic potentials qualitatively reproduce several of the spectral properties observed, such as the asymmetric bandshape, but display too little temperature dependence in the VT-absorption simulations and do not reproduce the experimental relative Raman intensities well.[47] The RREP simulations are improved by allowing $\Delta Q_1/\Delta Q_2$ to vary from 0.81, but no satisfactory simulated absorption data set can be generated. The calculations thus far have used identical ground- and excited-state potential parameters along each of the two a_1' normal coordinates. From the harmonic Raman analysis (*vide supra*), however, this excited state is known to undergo large distortions along these coordinates, and these distortions must be accompanied by force-constant and associated vibrational-frequency changes. After one allows for different ground- and excited-state vibrational frequencies, a solution ($\Delta x_1 \approx +0.105$, $\Delta x_2 \approx +0.082$) is found that fits all spectroscopic observables well. VT-absorption spectra using these parameters are compared to the experimental data on an expanded energy scale in Figure 6a, and the calculated RREPs for the 316 and 124 cm^{-1} modes are shown with the experimental data points in Figure 6b. The solution corresponds to a (+ +)-distorted excited state having relative dimensioned displacements of ∼1.2:1 along the $a_1'(1)$:$a_1'(2)$ normal coordinates. The simulation parameters used in Figure 6 are given in Table 5, where they are compared with the analogous results determined from the harmonic analysis. The coordinate displacements and the resulting excited-state geometric distortion parameters are presented in Table 6, and $(\partial V^{exp}_{ex}/\partial Q)_0$ values obtained from the L−J curves defined by these parameters are presented in Table 4 in comparison with the analogous $(\Delta E^{X\alpha}_{\sigma\rightarrow\sigma^*}/\Delta Q)_0$ values obtained from Xα−SW calculations (*vide supra*).

(D) Summary of Results from Harmonic and Anharmonic *σ* → *σ Excited-State Distortion Analyses.** The $a_1'(t_{2g}) \rightarrow a_2''(t_{2g})$ one-electron promotion in $[Fe_2(OH)_3(tmtacn)_2]^{2+}$ results in large geometric distortions, reflecting the significant contributions of the orbitals involved in this promotion to the geometries of the ground- and excited-states. In the FC region of the $a_1'(t_{2g}) \rightarrow a_2''(t_{2g})$ excited state the molecule experiences large forces along two a_1' core normal-coordinate directions that combine to elongate the Fe⋯Fe internuclear separation through Fe−OH bond length and Fe−O−Fe angle expansions. Comparison of the dimensioned displacement parameters in Table 5 derived from the anharmonic and harmonic analyses shows a general agreement between the two approaches, with the harmonic approximations leading to overestimated dimensioned displacements in both modes relative to those of the anharmonic analysis. The larger difference between the harmonic and anharmonic displacement magnitudes in the $a_1'(2)$ coordinate reflects the inability of the harmonic approach to accurately evaluate the contributions of low-frequency modes that contribute relatively little to the total absorption bandwidth, by which both displacements are scaled in the harmonic analysis, and the anharmonic analysis thus provides a more accurate description of the $a_1'(t_{2g}) \rightarrow a_2''(t_{2g})$ distorted excited-state geometry. Figure 7 summarizes schematically the results of the anharmonic-potential excited-state distortion analysis of the absorption and resonance Raman spectral features given in Table 6, depicting the $[Fe_2(OH)_3]^{2+}$ core distortion (in terms of atomic displacements relative to the ground-state equilibrium geometry) as arising from a + + combination of $a_1'(1)$ and $a_1'(2)$ normal-coordinate distortions and showing the dominant feature of the excited-state distortion to be an increase in the metal−metal separation. This result is consistent with the $\sigma \rightarrow \sigma^*$ description of this transition determined from a molecular orbital analysis of the electronic spectroscopy of $[Fe_2(OH)_3(tmtacn)_2]^{2+}$,[14] in which ∼82 to 97% of the energy of this excitation is attributed to a direct Fe−Fe σ-bonding interaction.

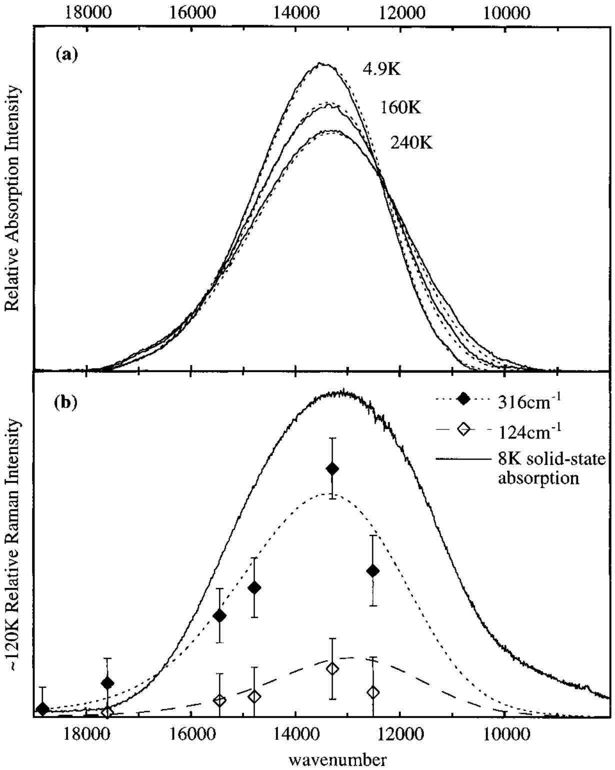

Figure 6. (a) Experimental (—) and simulated (- - -) variable-temperature solution near-IR absorption spectra and (b) experimental and simulated ∼120 K solid-state resonance Raman excitation profiles of the 316 (◆) and 124 cm^{-1} (◇) vibrational modes of $[Fe_2(OH)_3(tmtacn)_2]^{2+}$. Simulations are calculated using Lennard−Jones potentials and the parameters given in Table 5. The 8 K solid-state absorption spectrum is superimposed in part b.

Discussion

Roles of *Q*₋ and *Q*_{sym} in Absorption and Resonance Raman Spectra of Mixed-Valence Dimers. An important aspect of the vibronic analysis presented above is the observation that the $\sigma \rightarrow \sigma^*$ electronic absorption and resonance Raman spectra of $[Fe_2(OH)_3(tmtacn)_2]^{2+}$ are dominated by contributions from totally-symmetric nuclear coordinates and involve no discernible contribution from the symmetry-breaking $a_2''(Q_-)$

---

(47) In the case of a large excited-state distortion, eq 3 is no longer valid and a more accurate expression must be used. Comparison of RREPs calculated from eq A13 and eq 1 (which leads to eq 3) for the two-mode problem using large distortions reveals that the eq A13 RREPs have their maxima at higher energy than the eq 1 RREPs, and both the relative and absolute intensities differ between the two solutions.

Table 5. Summary of Results from the Analysis of Variable-Temperature Absorption and ∼120 K Resonance Raman Excitation Profile Data of $[Fe_2(OH)_3(tmtacn)_2]^{2+}$ and the Resulting $\sigma \rightarrow \sigma^*$ Excited-State Vibrational−Relaxation Energies, E_R, along each a_1' Normal Coordinate

Anharmonic Analysis[a]

Q_n	ν(gs), cm^{-1}	V_0(gs), cm^{-1}	γ	Δx	$\Delta Q/\delta$	ΔQ (Å)	ν(es), cm^{-1}	V_0(es), cm^{-1}	E_R, cm^{-1}
$a_1'(1)$	316.2	8876	300	+0.105	+4.20	+0.359	218.0	6122	3940
$a_1'(2)$	124.4	2618	225	+0.082	+2.84	+0.298	124.4	2618	875
									tot. 4815

Harmonic Analysis

Q_n	ν(gs), cm^{-1}	Δ (=$\Delta Q/\delta$)	ΔQ (Å)	ν(es), cm^{-1}	E_R, cm^{-1}
$a_1'(1)$	316.2	+5.09[b]	+0.434	316.2	4100
$a_1'(2)$	124.4	+5.09[b]	+0.534	124.4	1610
					tot. 5710

Single Effective Harmonic Mode Analysis

Q_n	ν_{eff}(gs), cm^{-1}	Δ_{eff} (=$\Delta Q_{eff}/\delta_{eff}$)	ν_{eff}(es), cm^{-1}	E_R, cm^{-1}
Q_{eff}	273	+6.32	273	5450

[a] See Appendix for description of calculation. Gaussian damping factors: $\alpha_1 = 372$, $\alpha_2 = 40$ (see Appendix). [b] Gives $S_1 = S_2 = 13$ from eq 5.

Table 6. $[Fe_2(OH)_3(tmtacn)_2]^{2+}$ $\sigma \rightarrow \sigma^*$ Excited State Distortions, Based on Calculated Normal Coordinate Descriptions and Distortion Parameters Obtained from Simulation of the Variable-Temperature Absorption and Resonance Raman Excitation Profile Data Using Anharmonic Potentials

		ground-state vibrational normal coordinates (Q_n)		excited-state internal-coordinate distortions (Δr_i(Å)) from L−J spectral analysis		
int coord	idealized ground-state geometry	+ $a_1'(1)$: 316 cm^{-1}	+ $a_1'(2)$: 124 cm^{-1}	+ $a_1'(1)$: 316 cm^{-1}	+ $a_1'(2)$: 124 cm^{-1}	$\sigma \rightarrow \sigma^*$ excited-state distortions from L−J spectral analysis + +
Fe⋯Fe	2.509 Å	0.1424	0.1246	0.1953	0.1842	+0.38 Å
Fe−OH	1.944 Å	0.1164	−0.0403	0.1597	−0.0596	+0.10 Å
Fe−O−Fe	80.38°	−0.0052	0.1189	−0.0071	0.1758	+0.17 (+9.4°)
O−Fe−O	82.84°	0.0039	−0.0886	0.0053	−0.1310	−0.13 (−7.1°)

Displacement from Origin with $\sigma \rightarrow \sigma$ Excitation

Fe	+0.19 Å
O	−0.04 Å
(ratio Fe:O)	(+4.9:−1.0)

vibrational coordinate (where Q_- in symmetrical (*i.e.* equal ligation) mixed-valence dimers is described as the out-of-phase combination of monomeric breathing motions: $Q_- = (1/2^{1/2})(Q_A - Q_B)$). In D_{3h} symmetry, coupling of a_2'' nuclear-coordinate displacements with dipole-allowed electronic excitations is group-theoretically forbidden, and this coordinate may contribute to the absorption and resonance Raman spectroscopy of this dimer through changes in excited-state potential-surface curvature (*i.e.* modal force constant) only. Equation 13[48] describes the effect of a change in excited-state harmonic curvature on the low-temperature single-coordinate absorption bandshape in terms of the percentage intensity remaining in the electronic origin (I_{0-0}) after such a change:

$$\frac{I_{0-0}}{I_{tot}} = \frac{2\sqrt{(\nu_{gr})(\nu_{ex})}}{\nu_{gr} + \nu_{ex}} = \frac{2\chi^{1/4}}{\chi^{1/2} + 1} \qquad (13)$$

where $\chi = (k_{ex}/k_{gr})$. In the limit of no curvature change along Q_- between ground and excited states (*i.e.* $\chi = 1$), 100% of the LT absorption intensity from Franck−Condon ground- and excited-state overlap along this coordinate is found in the electronic origin (0−0) band, and higher vibronic transitions (0−n) in the Q_- coordinate do not contribute to the absorption bandshape. As χ deviates from 1, orthogonality between the ground-state and additional Q_- vibronic excited-states ($n \neq 0$) is relaxed and new higher-energy vibronic transitions (0−n) are introduced to the absorption bandshape. Using the $a_2''(Q_-)$ frequency from Table 2, the electronic-coupling matrix element, H_{AB}, determined from absorption spectroscopy ($E_{\sigma\rightarrow\sigma^*} = 2H_{AB}$), and geometric parameters of ferric and ferrous monomers, ground- and excited-state Q_- potential surfaces have been calculated for the $\sigma \rightarrow \sigma^*$ transition in $[Fe_2(OH)_3(tmtacn)_2]^{2+}$, from which a value of $\chi \approx 1.5$ for the relative increase in Q_- vibrational force constant in the $\sigma \rightarrow \sigma^*$ excited state is obtained.[49] An excited-state force-constant increase of $\chi = 1.5$ with no potential displacement is seen from eq 13 to result in a shift of ∼0.5% of the total absorption intensity into vibronic transitions other than the 0−0 component of the electronic transition. An equally large shift of absorption intensity to higher vibronic transitions (0−n) is obtained from an excited-state potential displacement along a totally-symmetric coordinate having a Huang−Rhys parameter of only $S \approx 0.005$, which is over 3 orders of magnitude smaller than those observed experimentally for each of the two a_1' coordinates involved in the $\sigma \rightarrow \sigma^*$ excited-state distortion of $[Fe_2(OH)_3(tmtacn)_2]^{2+}$ ($S_1 \approx S_2 \approx 13$, Table 5). Similarly small $a_2''(Q_-)$ resonance Raman scattering intensities are obtained from this change in curvature *via* an Albrecht C-term mechanism.[50] Thus, the absorption and resonance Raman intensities resulting from the change in excited-state potential curvature along the $a_2''(Q_-)$

---

(48) Sponer, H.; Teller, E. *Rev. Mod. Phys.* **1941**, *13*, 75−106.

(49) The ground- and excited-state potential surfaces are calculated from the expression:

$$E = \frac{1}{2}\left(\frac{\lambda^2}{k_-}\right)x_-^{\,2} \pm \left[\frac{1}{2}\left(\frac{\lambda^2}{k_-}\right)^2 x_-^{\,2} + H_{AB}^{\,2}\right]^{1/2}$$

and the value of $\lambda^2/k_- = 2590$ cm^{-1}, derived from $\Delta r = 0.1$ Å, $\nu_- = 306$ cm^{-1}, and $\mu_- = 15.5$ g/mol.[14]

(50) Tang, J.; Albrecht, A. C. In *Raman Spectroscopy*; Szymanski, H. A., Ed.; Plenum: New York, 1970; Vol. 2, pp 33−68.

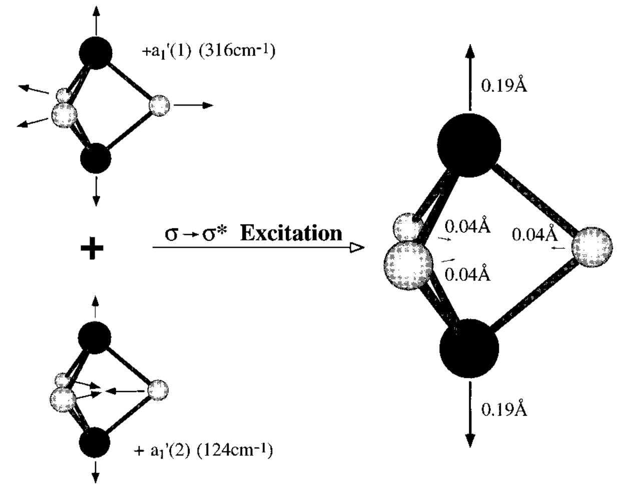

Figure 7. Nuclear distortion in the $\sigma \rightarrow \sigma^*$ excited state of $[Fe_2(OH)_3(tmtacn)_2]^{2+}$, arising from the + + combination of distortions along $a_1'(1)$ and $a_1'(2)$ normal coordinates. The figure is based on analysis of resonance Raman excitation profiles and variable-temperature absorption data, normal-coordinate vibrational descriptions, and $(\Delta E^{X\alpha}_{\sigma\to\sigma^*}/\partial Q)_0$ calculations.

normal coordinate in the $\sigma \rightarrow \sigma^*$ excited state of $[Fe_2(OH)_3(tmtacn)_2]^{2+}$ are calculated to be too small to be observed over the dominant effects of large distortions along the $a_1'(1)$ and $a_1'(2)$ totally-symmetric vibrational normal coordinates in this excited state.

Generalization of this observation provides valuable insight into the relationship between the vibronic spectroscopies of mixed-valence dimers and their valence delocalization properties. In class II localized dimers the Q_- nuclear coordinate is totally symmetric (for example, the a_2'' vibration in D_{3h} symmetry transforms as a_1 in C_{3v} symmetry), and nuclear distortions along the Q_- nuclear coordinate may therefore couple to dipole-allowed MMCT electronic transitions originating from the localized ground state. In a symmetrical class II mixed-valence dimer with relatively weak electronic coupling, MMCT (or IT) excitation promotes an electron from the reduced site to the oxidized site and thus involves a significant net geometric change along Q_-, the nuclear coordinate connecting the reduced and oxidized single-site geometries. Q_- may therefore contribute significantly to MMCT absorption bandshapes and Albrecht *A*-term resonance Raman intensities in class II dimers. In strongly-localized symmetrical class II dimers, MMCT excitations do not involve significant distortion along coordinates other than Q_-, and so their absorption bandwidths and resonance Raman intensities[51] are determined largely by the properties of the Q_- coordinate, namely the Q_- vibrational frequency and vibronic trapping parameter.[4,5] Representative potential surfaces illustrating the class II MMCT absorption process are depicted in Figure 8 for the Q_- (Figure 8a) and Q_{sym} (Figure 8b) coordinates in a symmetrical class II mixed-valence dimer, where Q_{sym} represents a linear combination of all other totally-symmetric normal coordinates.

As the electronic coupling between metal ions is increased, the MMCT transition shown in parts a and b of Figure 8 gains more dimer bonding-to-antibonding (or nonbonding) character. In the class III delocalized limit, the two metal ions are equivalent and the excited-state potential displacement along Q_- goes to zero, since the Q_- coordinate is not totally symmetric in the higher point group of the symmetrical delocalized dimer. Q_- is therefore normal Raman forbidden, and gains resonance Raman intensity only in even quanta from the change in excited-state curvature (*i.e.* force constant) by an Albrecht *C*-term mechanism. Alternatively, the changes in metal−metal and/or metal−bridging ligand bonding interactions accompanying the class III $\psi \rightarrow \psi^*$ transitions of delocalized dimers result in displaced potentials along totally-symmetric nuclear coordinates (Q_{sym}) in the excited state and these coordinates thus contribute to the class III $\psi \rightarrow \psi^*$ absorption bandwidth and resonance Raman scattering *via* an excited-state potential-displacement mechanism (Albrecht *A*-term in RR). These absorption processes are depicted in Figure 8 for vibronic excitations along the Q_- (Figure 8c) and Q_{sym} (Figure 8d) coordinates in a symmetrical class III dimer. As described by eq 13, changes in curvature do not effectively contribute to absorption band-broadening, and consequently even a small Q_{sym} distortion will overshadow the Q_- contribution to the absorption and resonance Raman intensities in class III mixed-valence systems.

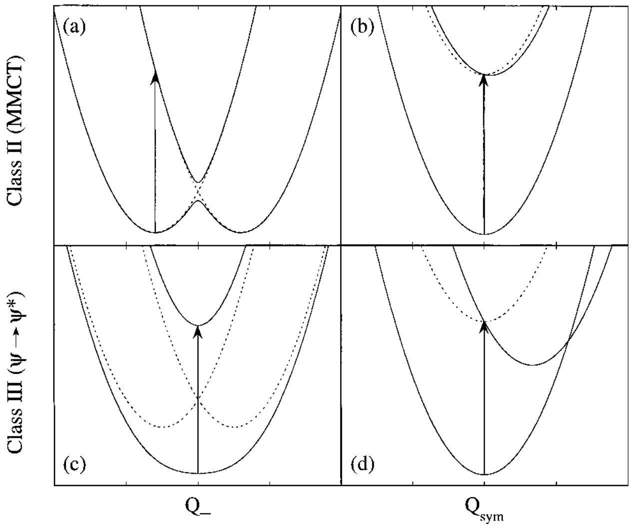

Figure 8. Vibronic transitions involving Q_- and Q_{sym} nuclear coordinates in class II and class III mixed-valence dimers, based on the excited-state spectroscopy of $[Fe_2(OH)_3(tmtacn)_2]^{2+}$. Comparison of excited-state $\partial V/\partial Q$ values in the Franck−Condon overlap regions of each illustrates the dominant role of (a) Q_- in the vibronic spectroscopy of class II dimers and (d) Q_{sym} in the vibronic spectroscopy of class III dimers (see text). Q_{sym} refers to an effective symmetric-distortion coordinate, which in $[Fe_2(OH)_3(tmtacn)_2]^{2+}$ is the linear combination of $a_1'(1)$ and $a_1'(2)$ vibrational normal coordinates shown in Figure 7.

An analogous effect has been proposed previously in relation to the near-IR absorption feature of the class III mixed-valence Creutz−Taube ruthenium dimer.[6−8,52,53] This interpretation of the absorption bandshape is supported by recent near-IR resonance Raman experiments in which enhancement of totally-symmetric vibrations dominates the observed spectra,[54] consistent with the spectroscopy anticipated from the ground- and excited-state class III Q_- and Q_{sym} potentials depicted in Figure 8c,d. The large disparity in magnitude between the contributions of coordinate displacement vs change in curvature to absorption band broadening suggests that excited-state distortions along totally-symmetric coordinates may be generally anticipated to dominate the absorption and resonance Raman spectroscopy of all class III mixed-valence systems in which large electronic coupling limits the bandshape contribution of the Q_- coordinate exclusively to a change-in-curvature mechanism. Indeed,

---

(51) See for example: Clark, R. J. H. *Chem. Soc. Rev.* **1984**, 219−244.

(52) Hush, N. S. In *Mixed-Valence Compounds*; Brown, D. B., Ed.; D. Reidel Pub. Co.: Dordrecht, The Netherlands, 1980; pp 151−188.

(53) Hush, N. S. In *Mechanistic Aspects of Inorganic Reactions*; Rorabacher, D. B., Endicott, J. F., Eds.; ACS Symposium Series 198; American Chemical Society: Washington DC, 1982; pp 301−329.

(54) Petrov, V.; Hupp, J. T.; Mottley, C.; Mann, L. C. *J. Am. Chem. Soc.* **1994**, *116*, 2171−2172.

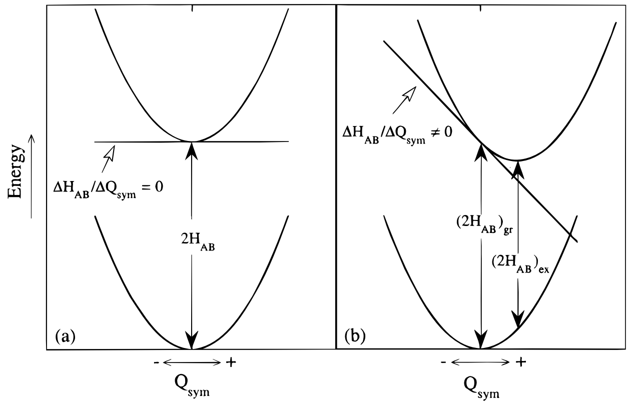

Figure 9. Generalized mechanism for the structural dependence of the inter-ion electronic-coupling matrix element, H_{AB}, in mixed-valence dimers. (a) The class III $\psi \rightarrow \psi^*$ excited-state is not distorted and the separation between ground and excited states is independent of Q_{sym} (*i.e.* $\Delta H_{AB}/\Delta Q_{sym} = 0$). (b) The separation between ground and excited states is decreased in the class III $\psi \rightarrow \psi^*$ excited-state equilibrium geometry relative to the ground-state value due to excited-state distortion along Q_{sym}, resulting in a geometry-dependent H_{AB} (*i.e.* $\Delta H_{AB}/\Delta Q_{sym} \neq 0$). Panel b corresponds to the case presented in Figure 8d.

examples of class III $\psi \rightarrow \psi^*$ resonance Raman spectroscopy of other delocalized mixed-valence dimers show resonance Raman intensity dominated by multiple totally-symmetric vibrations,[55-57] allowing a similar conclusion to be drawn about their absorption profiles.

Structural Dependence of the Electronic-Coupling Matrix Element, H_{AB}. From inspection of the potential surfaces shown in Figure 8d it is evident that class III $\psi \rightarrow \psi^*$ excited-state distortions result in a strong geometry dependence of the energy splitting between the ground and excited states. This in turn reflects a structural dependence of the electron-transfer matrix element, H_{AB}, since $E_{\psi \rightarrow \psi^*} = 2H_{AB}$ in these transitions. The parameters (Table 5) of the anharmonic-potential surfaces used to simulate the 13 500 cm^{-1} $\sigma \rightarrow \sigma^*$ absorption and resonance Raman data of $[Fe_2(OH)_3(tmtacn)_2]^{2+}$ can be used to quantify the structural dependence of H_{AB} in this dimer: Summing the ground- and excited-state vibrational-relaxation energies that result from the nuclear distortion shown in Figure 7 yields a $\sigma - \sigma^*$ splitting energy of $E_{\sigma \rightarrow \sigma^*} = 6850$ cm^{-1} at the excited-state equilibrium geometry, and an average value of $\Delta E_{\sigma \rightarrow \sigma^*}/\Delta r_{Fe-Fe} = (13\,500 - 6850 \text{ cm}^{-1})/0.38 \text{ Å} = 17\,520 \text{ cm}^{-1}/\text{Å}_{Fe-Fe}$ over the entire range between ground- and excited-state equilibrium geometries, indexed to the Fe···Fe separation. This corresponds to a value of $\Delta H_{AB}/\Delta r_{Fe-Fe} = 8760 \text{ cm}^{-1}/\text{Å}_{Fe-Fe}$ over this range. The structural dependence of H_{AB} observed in $[Fe_2(OH)_3(tmtacn)_2]^{2+}$ is generalized in Figure 9b, where Q_{sym} represents any effective symmetric distortion coordinate, as in Figure 8. The significant variation of H_{AB} in $[Fe_2(OH)_3(tmtacn)_2]^{2+}$ with structural changes that predominantly involve the Fe···Fe separation directly reflects the effects of these changes on the delocalization pathway of this dimer, namely the d_{z^2}-d_{z^2} σ-bonding interaction.[14]

Anharmonicity and VT-Absorption BandShapes. Finally, a description of the effects of potential-surface anharmonicity on absorption bandshapes has been presented which shows that, in cases where large excited-state distortions occur, anharmonicity is expected to contribute significantly to the absorption bandshape. The greatest effects occur when the excited state is displaced in a positive ($\Delta x > 0$) direction relative to the ground state, and this is seen to generate asymmetric bands at low temperatures (Figure 5) rather than the symmetric bandshapes predicted by harmonic theory for excitations involving large excited-state distortions. In addition, excited-state anharmonicity also leads to a large temperature-dependent asymmetry of the absorption bandshape (when sufficient population of excited vibrational levels is accessible, Figure 5b), attributable to the large $(\partial V_{ex}/\partial Q)_0$ and increasing density of states in the FC region of the anharmonic excited-state surface. The observation of anharmonic effects in the absorption spectrum can also allow determination of the direction of excited-state potential displacement due to the large differences in these effects between comparable positive and negative excited-state displacements.

Acknowledgment. The authors thank L. B. LaCroix and D. E. Root for assistance with the Xα−SW calculations. E.I.S. thanks the NSF Biophysics program (Grant MCB9316768) for support of this research. E.L.B. gratefully acknowledges financial support by the National Institutes of Health (Grant GM22701) to Dr. E. Münck.

Appendix: Calculation of Temperature-Dependent Absorption Bandshapes and Resonance Raman Excitation Profiles Using Anharmonic Potentials

Simulation of the temperature-dependent absorption and resonance Raman data is accomplished by substitution of Franck−Condon overlap factors, $\langle i|v\rangle^2$, calculated from solutions[45] of the dimensionless Schrödinger equation for anharmonic potentials (eq 11b) into expressions for temperature-dependent light absorption and resonance Raman scattering intensities.

Absorption. The absorption cross section for dipole-allowed transitions can be written in the Born−Oppenheimer and Condon approximations as

$$\sigma_{abs} = \frac{4\pi^2 e^2 M^2}{3\hbar c} E_{ex} g_n(E_{ex}) \qquad \text{(A1)}$$

where M is the electronic transition length, E_{ex} is the energy of excitation in cm^{-1}, and $g_n(E_{ex})$ is a temperature-dependent bandshape function which, for a single promoting mode ($n = 1$), is given by

$$g_1(E_{ex}) = \frac{1}{Z}\sum_i \left\{ \exp\left[\frac{-\epsilon_i}{kT}\right] \sum_v \langle i|v\rangle^2 G_\alpha(\epsilon_v - \epsilon_i - E_{ex}) \right\} \qquad \text{(A2)}$$

where Z is the partition function describing the temperature-dependent Boltzmann population distribution over the various vibrational levels:

$$Z = \sum_i \exp[-\epsilon_i/kT] \qquad \text{(A3)}$$

Single transitions between the vibrational levels of the ground state ($|i\rangle$) and the excited state ($|v\rangle$), at energies ϵ_i and ϵ_v, are described by a Gaussian bandshape function

$$G_\alpha(E) = \sqrt{\frac{\alpha}{\pi}} \exp(-\alpha E^2) \qquad \text{(A4)}$$

where α is the Gaussian damping factor. As shown in eq A2, the transitions are weighted by FC factors, which are the squares of the overlap integrals obtained numerically for the displaced L−J potentials as described in the Analysis section of the text.

---

(55) Armstrong, R. S.; Beattie, J. K.; Del Favero, P.; Ellis, V. M.; Hush, N. S. *Inorg. Chem. Acta* **1984**, *89*, L33−L34.

(56) Farrar, J. A.; McKee, V.; Al-Obaidi, A. H. R.; McGarvey, J. J.; Nelson, J.; Thomson, A. J. *J. Am. Chem. Soc.* **1995**, *34*, 1302−1303.

(57) Dong, Y.; Fujii, H.; Hendrich, M. P.; Leising, R. A.; Pan, G.; Randall, C. R.; Wilkinson, E. C.; Zang, Y.; Que, L., Jr.; Fox, B. G.; Kauffmann, K.; Münck, E. *J. Am. Chem. Soc.* **1995**, *117*, 2778−2792.

The simulation procedure for the absorption spectrum using L−J potentials is facilitated by using an approximate relationship between the coordinate shift and the bandwidth. In the harmonic approximation, eq 4 is used to describe the absorption fwhm in terms of frequencies and dimensionless displacements. In the single-mode case, dividing eq 4 by ν gives

$$\frac{\text{fwhm}}{\nu} = (4\sqrt{2}\ln 2)\frac{|\Delta Q|}{\Delta_{1/2}} = 2\sqrt{\ln 2}|\Delta| \qquad \text{(A5)}$$

where

$$\Delta_{1/2} = 2\delta\sqrt{2\ln 2}$$

is the fwhm of the $v = 0$ ground-state vibrational wavefunction and

$$\delta \equiv \sqrt{\frac{\nu}{k}}$$

as described in the Analysis section. The expression roughly states that the number of vibrational quanta that fit in the bandwidth is proportional to the number of ground-state wavefunctions that are needed to cover the coordinate shift, ΔQ (Å). Thus, in the harmonic limit the quantity Δ is obtainable from experimental values for ν and fwhm, as described in the Analysis section. The corresponding expression for a L−J potential is given in eq A6. Using eq A6 and an estimated

$$\frac{\text{fwhm}}{\nu} = \frac{1}{6}\sqrt{\frac{\gamma\ln 2}{3(2^{1/2})}}\left|\left(\frac{\mathrm{d}V_{\mathrm{ex}}}{\mathrm{d}x}\right)_0\right| \qquad \text{(A6)}$$

value for γ (eqs 11, 12), a value for $|(\partial V_{\mathrm{ex}}/\partial x)_0|$ can be inferred from the experimental data for fwhm and ν (where the subscript 0 denotes $x_{0,\mathrm{gr}}$). From this, the value for the dimensionless shift, Δx, and hence ΔQ (Å), can be determined from numerical analysis of the L−J $(\partial V_{\mathrm{ex}}/\partial x)_0$ function.

Extension of eqs A2 and A6 to accommodate distortion along two normal coordinates ($n = 2$) yields the two-mode temperature-dependent bandshape function

$$g_2(E_{\mathrm{ex}}) = \frac{1}{Z_{1,2}}\sum_{i_1,i_2}\left\{\exp\left[\frac{-(\epsilon_{i_1}^{(1)} + \epsilon_{i_2}^{(2)})}{kT}\right]\right.$$
$$\left.\sum_{v_1,v_2}\langle i_1|v_1\rangle^2\langle i_2|v_2\rangle^2 G_\alpha(\epsilon_{v_1}^{(1)} + \epsilon_{v_2}^{(2)} - \epsilon_{i_1}^{(1)} - \epsilon_{i_2}^{(2)} - E_{\mathrm{ex}})\right\} \qquad \text{(A7)}$$

and L−J bandwidth expression

$$\Delta E = \frac{1}{6}\sqrt{\frac{\ln 2}{3(2^{1/2})}}\left[\gamma_1\nu_1^{\,2}\left(\frac{\delta V_{1,\mathrm{ex}}}{\delta x_1}\right)_0^2 + \gamma_2\nu_2^2\left(\frac{\delta V_{2,\mathrm{ex}}}{\delta x_2}\right)_0^2\right]^{1/2} \qquad \text{(A8)}$$

Note that in the two-mode problem

$$Z_{1,2} = \sum_{i_1,i_2}\exp[-(\epsilon_{i_1}^{(1)} + \epsilon_{i_2}^{(2)})/kT] =$$
$$(\sum_{i_1}\exp[-\epsilon_{i_1}^{(1)}/kT])(\sum_{i_2}\exp[-\epsilon_{i_2}^{(2)}/kT]) = Z_1 Z_2 \qquad \text{(A9)}$$

such that the Boltzmann population distributions for the two modes in eq A7 can be normalized independently of one another. Computationally it is more efficient to calculate the bands for the two modes (g_1 and g_1') individually, and simulate the total two-mode absorption from these using the convolution integral presented in eq A10. For simplicity, the absorption energy axes

$$g_2(E_0) \approx \int_{-\infty}^{\infty} g_1(E_0 - E)g_1'(E)\,\mathrm{d}E \qquad \text{(A10)}$$

are shifted in the calculation such that $E_{0-0} = 0$ using $E_0 = E_{\mathrm{ex}} - E_{0-0}$, and the resulting curves reshifted by the experimental E_{0-0} value. The accuracy of this procedure has been verified by application of the convolution and direct calculational procedures to the same set of displaced L−J potential parameters. Excellent agreement between the results using the two methods is observed.

Resonance Raman. The total resonance Raman scattering at given excitation (E_{ex}) and scattering (E_{scat}) photon energies is $I_s = P\sigma_{\mathrm{RR}}$, where I_s is the scattered power (photons/s) and P is the incident excitation intensity (photons/cm^2 s). σ_{RR} is the resonance Raman cross section described by the Kramers−Heisenberg−Dirac expression, summed over all directions and polarizations of scattered radiation, as

$$\sigma_{\mathrm{RR}} = \frac{8\pi}{9}\frac{E_{\mathrm{scat}}{}^3 E_{\mathrm{ex}} e^4 M^4}{\hbar^4 c^4}h_{\mathrm{RR}}(E_{\mathrm{ex}}) \qquad \text{(A11)}$$

where E_{scat} is the energy of the scattered photon, E_{ex} the energy of the excitation photon, M is the electronic transition length, and $h_{\mathrm{RR}}(E_{\mathrm{ex}})$ is the bandshape function. The single-mode Albrecht A-term[50] resonance Raman bandshape function for finite temperatures is given by

$$h_{\mathrm{RR}}{}^{n}(E_{\mathrm{ex}}) = \frac{1}{Z}\sum_j \exp\left(-\frac{\epsilon_j}{kT}\right)\left|\sum_v \frac{\langle j+n|v\rangle\langle v|j\rangle}{\epsilon_v - \epsilon_j - E_{\mathrm{ex}} + i\Gamma}\right|^2 \qquad \text{(A12)}$$

where overlap integrals, $\langle i|v\rangle$, are obtained numerically from the displaced L−J potentials as described in the Analysis section of the text.

The two-mode temperature-dependent resonance Raman bandshape function follows from a straightforward generalization of the single-mode function analogous to that of the absorption calculations, yielding

$$h_{\mathrm{RR}}{}^{n_1,n_2}(E_{\mathrm{ex}}) = \frac{1}{Z_{1,2}}\sum_{i_1,i_2}\exp[-(\epsilon_{i_1}^{(1)} +$$
$$\epsilon_{i_2}^{(2)})/kT]\left|\sum_{v_1,v_2}\frac{\langle i_1+n_1|v_1\rangle\langle i_2+n_2|v_2\rangle\langle v_1|i_1\rangle\langle v_2|i_2\rangle}{\epsilon_{v_1}^{(1)} + \epsilon_{v_2}^{(2)} - \epsilon_{i_1}^{(1)} - \epsilon_{i_2}^{(2)} - E_{\mathrm{ex}} - i\Gamma}\right|^2 \qquad \text{(A13)}$$

If the ground- and excited-state potentials are approximated as harmonic and having equal force constants, in the limit of small coordinate displacements ($\Delta Q < \delta$) and low temperatures ($kT \ll \nu$) all overlap integrals other than

$$\langle 1|0\rangle = -\langle 0|1\rangle \approx \frac{\Delta}{\sqrt{2}}$$

can be ignored leading to the approximate single-mode resonance Raman bandshape function presented by Blazej and Peticolas[31] and given in eq 1 (where $\Delta = \Delta Q/\delta$), from which eq 3 is obtained describing the relative intensities of two modes in the preresonance region.[47]

Supporting Information Available: Listings of input parameters for SCF−Xα−SW calculations and NCA force-field output parameters (1 page). Ordering information is given on any current masthead page.

IC960413U